Applied Surface Science 481 (2019) 1196–1205

Contents lists available at ScienceDirect

Applied Surface Science

journal homepage: www.elsevier.com/locate/apsusc

Full length article

Scalable synthesis of high-performance molybdenum diselenide-graphite nanocomposite anodes for lithium-ion batteries

Hyeongi Kim[a,1], Quoc Hai Nguyen[a,b,1], Il Tae Kim[a,*], Jaehyun Hur[a,*]

[a] Department of Chemical and Biological Engineering, Gachon University, Seongnam, Gyeonggi 13120, Republic of Korea
[b] Department of Chemical Technology, Baria-Vungtau University, Vietnam

ARTICLE INFO

Keywords:
Molybdenum diselenide
High-energy mechanical milling
Graphite
Solid lubrication
Anode
Lithium-ion batteries

ABSTRACT

Molybdenum diselenide-based carbon composites were prepared by a high-energy mechanical milling (HEMM) for anodes in lithium-ion batteries. In this paper, we have reported the effect of the type of carbonaceous matrix, for example, 2D graphite, 1D carbon nanotube, and 0D amorphous carbon, on the performance of $MoSe_2$-carbon nanocomposite anodes. The combination of $MoSe_2$ and graphite showed the best electrochemical performance in terms of cycling stability and rate capability. This improvement is associated with the increased surface area along both lateral and vertical directions of $MoSe_2$, and effective mixing between $MoSe_2$ and graphite due to HEMM. The facile exfoliation, size reduction, and homogeneous mixing of $MoSe_2$ upon the addition of graphite, were characterized by XRD, Raman spectroscopy, BET, SEM, and TEM. The $MoSe_2$-graphite nanocomposite ((2D)$MoSe_2$@(2D)Gr) exhibited enhanced Li storage (a reversible discharge capacity of 909 mAh g^{-1} at 100 mA g^{-1} after 200 cycles) and rate performance (611 mAh g^{-1} at a current density of 3 A g^{-1}) as compared to other $MoSe_2$-carbon nanocomposites, as well as pure $MoSe_2$. The reduced charge transfer resistance, increased diffusivity, and improved mechanical stability as confirmed by electrochemical impedance spectroscopy (EIS) and ex-situ SEM, further served to demonstrate the superiority of the (2D)$MoSe_2$@(2D)Gr electrode.

1. Introduction

Molybdenum diselenide ($MoSe_2$) is a member of the family of transition metal dichalcogenide-based two-dimensional (2D) materials, which are composed of stacked atomic layers (Se-Mo-Se) held by weak van der Waals forces [1]. Similar to other 2D materials, $MoSe_2$ exhibits very interesting properties such as intercalation, lubrication [2,3], and catalytic activity [4,5], resulting from its unique structure. Therefore, several studies demonstrated the varied applications of 2D materials in diverse areas including sensors [6,7], transistors [8–10], lubricants [11–14], catalysis, hydrogen storage, and energy storage [15,16]. Among the different 2D materials, $MoSe_2$ is one of the most promising candidates for use as an anode in lithium-ion batteries (LIBs) because of its relatively high theoretical capacity (422 mAh g^{-1}) and a larger interlayer spacing (0.65 nm) than graphite (0.33 nm) [17], which permits the facile insertion and desorption of ions (e.g., lithium and sodium) in an electrochemical reaction [17–20].

Owing to these advantages, $MoSe_2$ has been intensely studied in order to apply it as an anode material for secondary batteries. Liu et al. synthesized sheet-like $MoSe_2$ using a hydrothermal method and demonstrated a capacity of 576 mAh g^{-1} after 50 cycles at a current density of 100 mA g^{-1} [21]. The hydrothermal process was also used by Zhang et al. to prepare hierarchical $MoSe_2$ nanosheets, which showed a specific capacity of 917 mAh g^{-1} after 100 cycles at 0.5 A g^{-1} [17]. Shi et al. introduced a mesoporous silica SBA-15 template to synthesize mesoporous $MoSe_2$ via nanocasting, which exhibited a specific capacity of 630 mAh g^{-1} after 35 cycles at a current density of 0.05 C [22]. More recently, Wu et al. have successfully fabricated $MoSe_2$ hollow nanospheres via hydrothermal processing followed by an annealing treatment (specific capacity 744 mAh g^{-1} after 300 cycles at 1 A g^{-1}) [23]. In addition, the synthesis of hierarchical $MoSe_2$ yolk-shell microspheres by spray pyrolysis of MoO_3 and selenization of yolk-shell-structured MoO_3 were reported by Ko et al. [24], and fullerene-like $MoSe_2$ nanoparticle-embedded carbon nanotube (CNT) balls were fabricated using a similar approach by Choi et al. [25].

Despite these important advances, there are still several crucial issues that need to be resolved before $MoSe_2$ can be used as a battery anode. First, little is known of the effect of the carbon matrix on the structural characteristics and electrochemical performance of $MoSe_2$. In general, it is necessary to use some type of carbonaceous matrix (e.g.,

* Corresponding authors.
E-mail addresses: itkim@gachon.ac.kr (I.T. Kim), jhhur@gachon.ac.kr (J. Hur).
[1] H. Kim and Q. H. Nguyen contributed equally to this work.

https://doi.org/10.1016/j.apsusc.2019.03.165
Received 27 August 2018; Received in revised form 20 February 2019; Accepted 16 March 2019
Available online 18 March 2019
0169-4332/

amorphous carbon, graphene, reduced graphene oxide or CNT) as an additive to the active material to improve its electrochemical performance. This is because, the carbonaceous matrix can reduce the volumetric expansion of the $MoSe_2$ electrode and enhance the electrical conductivity of the $MoSe_2$ electrode, thereby reducing the physical stress, pulverization, and aggregation that occur during lithiation/delithiation. Despite much effort in this direction, the effect of the carbon matrix has not been satisfactorily addressed in a systematic way thus far. The detailed knowledge obtained based on these experiments will be beneficial to understanding the mechanism of the electrochemical reaction and will thus aid the development of new electrode materials with improved performance. Secondly, the processes adopted in most of the previous studies are somewhat complicated and therefore, difficult to upscale for mass production [26,27].

Herein, we propose a $MoSe_2$-graphite nanocomposite as a new high-performance anode for LIBs, prepared using high-energy mechanical milling (HEMM). The superiority of the $MoSe_2$-graphite nanocomposite electrode is demonstrated by systematically studying the effect of the type of carbon matrix by comparing carbonaceous additives of three different dimensions (e.g., 2D graphite, 1D CNT, and 0D carbon), on the structural and electrochemical characteristics of the $MoSe_2$-based electrode, as well as by comparing its performance with a carbon-free $MoSe_2$ electrode. Since the HEMM process adopted in our approach is very simple and can be easily scaled up (i.e., production of gram-quantities at a time), it can be potentially used for commercial production. The $MoSe_2$-graphite nanocomposite synthesized via HEMM exhibited the best cycling performance (a specific capacity of 909 mAh g^{-1} after 200 cycles at a current density of 100 mA g^{-1}) and rate capability (611 mAh g^{-1} at a current density of 3 A g^{-1}).

2. Experimental section

2.1. Materials

Molybdenum diselenide ($MoSe_2$, 325 mesh, 99.9%, Sigma-Aldrich), graphite powder (Gr, 100 mesh, Sigma-Aldrich), amorphous carbon black Super-P (C, ~40 nm 99.99%, Alfa Aesar), and multi-walled carbon nanotubes (CNTs, > 90%, Sigma-Aldrich) were used as-purchased without any further treatment.

2.2. Preparation of $MoSe_2$-carbon composites

$MoSe_2$-carbon composites were prepared by HEMM using a planetary ball-milling machine (Pulverisette 5, Fritsch). Three mixtures of $MoSe_2$ with different types of carbon powders (2D Gr, 1D CNT, 0D C) were prepared; the weight ratio of $MoSe_2$ to C was 7:3 in all the mixtures. The mixtures were placed in a zirconium oxide bowl (capacity of 80 cm^3) and mixed, using zirconium oxide balls of two different sizes (diameters of 3/8 and 3/16 in.). The weight ratio of the powder to the zirconia balls was 1:20, and the mixing bowls were assembled under Ar atmosphere in a glove box. The powder mixture was milled for various times (1, 12, 24, 36, 48, and 60 h) with a 30 min rest after every 1 h of milling, at a bowl-rotating speed of 300 rpm. As a control sample, bare $MoSe_2$ was also milled under the same conditions without adding carbon.

2.3. Characterization

The crystalline structures of the as-prepared samples were analyzed using X-ray diffraction (XRD); the XRD scans were acquired in the 2θ range 10–80° at a scan rate of 2° min^{-1}. (D/MAX-2200 Rigaku, Japan). Raman spectra of the samples were acquired using a Raman spectrometer (DXR Raman Microscope, 532 nm laser excitation). The morphology and structure of the $MoSe_2$-carbon composites were imaged using both scanning (SEM, Hitachi S4700, Japan) and transmission (TEM, TECNAI G2F30) electron microscopy. Elemental mapping images were obtained using energy dispersive spectroscopy (EDS) during TEM analysis. Brunauer-Emmett-Teller (BET) analysis was performed to measure the specific surface area and pore size distribution (ASAP 2020, Micromeritics, USA).

2.4. Electrochemical measurements

Electrochemical measurements were performed using coin-type cells (CR 2032). The working electrode was fabricated by casting a slurry containing 70% active material ($MoSe_2$-based nanocomposite), 15% conductive carbon black (Super-P), 15% polyvinylidene fluoride, and *N*-methyl-2-pyrrolidinone. The as-prepared solution was stirred at a constant speed for 12 h, after which the slurry was coated uniformly on a copper foil by doctor blading. The coated film was dried overnight in a vacuum oven at 70 °C. The electrode was then punched into a circular disc of 12 mm diameter. The coin-type cell was assembled under Ar atmosphere in a glove box. The electrolyte, reference electrode, and separator were 1 M $LiPF_6$ in ethylene carbonate/diethylene carbonate (1:1 in volume), lithium foil, and polyethylene, respectively. Galvanostatic electrochemical charge-discharge measurements were performed using a battery cycle tester (WBCS3000, WonAtech) in the voltage range 0.0–3.0 V vs. Li/Li^+ at various current densities. Cyclic voltammetry (CV) was performed using ZIVE MP1 (WonAtech) in the same voltage range at the scanning rate of 0.1 mV s^{-1}. Electrochemical impedance spectroscopic (EIS) measurements were carried out using ZIVE MP1 (WonAtech) with a 10 mV ac amplitude in the frequency range 100 mHz–100 kHz at the 10th cycle.

3. Results and discussion

Fig. 1 shows the XRD patterns of the ball-milled $MoSe_2$ and different $MoSe_2$-carbon (hereafter denoted as (2D)$MoSe_2$@(2D)Gr, (2D)$MoSe_2$@(1D)CNT, and (2D)$MoSe_2$@(0D)C) nanocomposites. The major peaks located at 2θ values of 13.6°, 31.4°, 37.8°, 47.4°, and 55.9° for all the $MoSe_2$-carbon nanocomposites correspond, respectively, to the (002), (100), (103), (105) and (110) planes of hexagonal $MoSe_2$ (PDF#

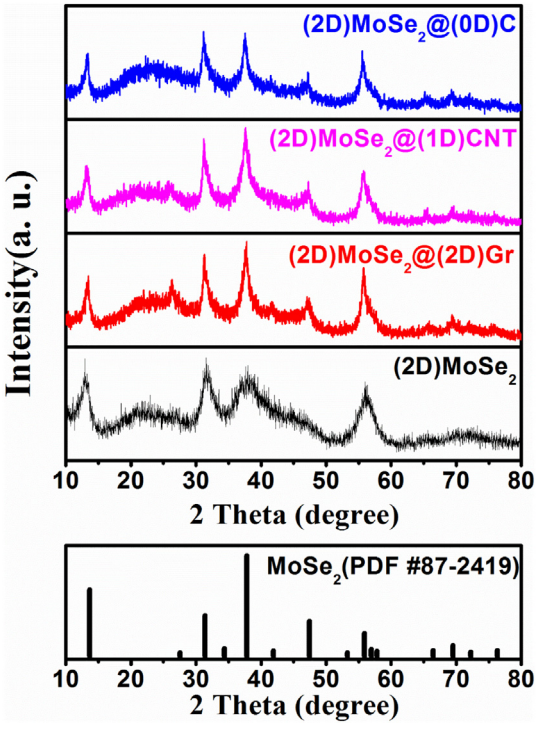

Fig. 1. XRD patterns of the bare $MoSe_2$ and $MoSe_2$-carbon composites after HEMM.

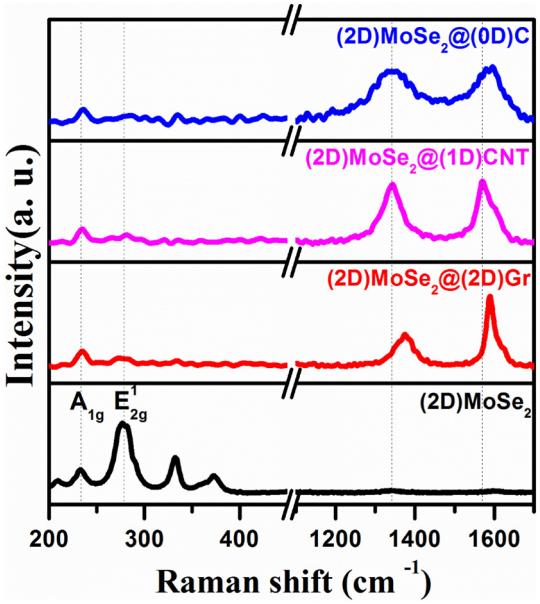

Fig. 2. Raman spectra of $MoSe_2$ and $MoSe_2$-carbon composites after HEMM.

87-2419). The peak at 26.5° seen in the (2D)$MoSe_2$/(2D)Gr originates from the (002) plane of graphite (PDF# 75-1621). No other impurity peaks are seen in all samples. The peak intensities and width for all the $MoSe_2$-carbon nanocomposites are not much different from those for $MoSe_2$ after HEMM, suggesting that the addition of carbonaceous materials does not decrease the crystallinity of $MoSe_2$.

The structural characteristics of $MoSe_2$ and $MoSe_2$-carbon nanocomposites following HEMM were further characterized by Raman spectroscopy (Fig. 2). The peaks at frequencies < 400 cm^{-1} correspond to $MoSe_2$, while those > 1200 cm^{-1} correspond to the D- and G-bands of the carbon material. The frequency difference between the two Raman peaks ($\Delta = A_{1g} - E_{2g}{}^1$) can be used to identify the average number of $MoSe_2$ layers [19,28]. We obtained Δ values of 47 ((2D)$MoSe_2$), 37 ((2D)$MoSe_2$@(2D)Gr), 44 ((2D)$MoSe_2$@1D CNT, and 51 ((2D)$MoSe_2$@(0D)C), indicating that the (2D)$MoSe_2$@(2D)Gr composite has the lowest number of $MoSe_2$ layers. This result also demonstrates the high degree of exfoliation of $MoSe_2$ in the presence of graphite during HEMM, which is attributed to the synergetic solid lubrication effect between $MoSe_2$ and graphite [29]. In general, it is well-known that most 2D materials easily undergo sliding under shear stress because of the relatively weak bonding between the individual layers of the basal planes [12,13,30]. Mechanical milling serves to apply shear stress on both the 2D materials, leading to greater exfoliation and a larger number of edge-terminated sites for $MoSe_2$ [31]. The presence of these sites is highly advantageous in electrochemical reactions because of the greater number of active sites in $MoSe_2$ which react with lithium ions. The Raman peaks located at ~1341 and 1566 cm^{-1} correspond, respectively, to the D-(disorder) and G-(crystalline) bands of carbon [32–41]. The intensity ratios (I_D/I_G) between these peaks is the lowest (0.46) for (2D)$MoSe_2$@(2D)Gr (0.92 for (2D)$MoSe_2$@(1D)CNT and 0.94 for (2D)$MoSe_2$@(0D)C), suggesting that the (2D)$MoSe_2$@(2D)Gr nanocomposite retains the high crystallinity of the graphite lattice with few defects and a low degree of disorder.

Fig. 3 presents the SEM images of $MoSe_2$ and $MoSe_2$-carbon nanocomposites. Although the particle sizes of the $MoSe_2$-based nanocomposites are all different, a uniform reduction in their average sizes is seen after HEMM, as compared to the particle sizes of the raw materials before HEMM. For example, the particle sizes of (2D)$MoSe_2$@(2D)Gr are in the range of 150 nm to a few μm after HEMM (Fig. 3b), which is much smaller than the original particle size of $MoSe_2$ (325 mesh, 44 μm) and graphite (100 mesh, 149 μm) before HEMM. The average particle size of (2D)$MoSe_2$@(0D)C appears to be the lowest (Fig. 3d), since the particle size of the starting 0D carbon is very low (~40 nm). The average particle size decreases in the order (2D)$MoSe_2$, (2D)$MoSe_2$@(2D)Gr, (2D)$MoSe_2$@(1D)CNT, and (2D)$MoSe_2$@(0D)C. This result reveals that the lateral particle size reduction is facilitated by the presence of carbon during HEMM; this contributes to the increase in the surface area of the composite.

The surface areas and pore sizes of $MoSe_2$ and $MoSe_2$-carbon composites were further examined using BET analyses. Fig. 4 displays the N_2 adsorption-desorption isotherms and pore size distributions of $MoSe_2$ and $MoSe_2$-carbon composites after HEMM. The values of the specific surface area and average pore size are listed in Table 1. The BET surface areas of $MoSe_2$ and (2D)$MoSe_2$@(2D)Gr after HEMM were calculated to be 11.14 $m^2 g^{-1}$ and 70.68 $m^2 g^{-1}$, respectively, which are considerably higher than those before HEMM (4.58 $m^2 g^{-1}$ for $MoSe_2$ and 3.43 $m^2 g^{-1}$ for (2D)$MoSe_2$@(2D)Gr, (Table 1 and Fig. S1)). Notably, the increase in surface area for (2D)$MoSe_2$@(2D)Gr is much higher than that for bare $MoSe_2$ after HEMM. This result points to the effective and synergetic mixing in the lateral direction as well as the facile exfoliation of 2D $MoSe_2$ and 2D graphite during HEMM. However, (2D)$MoSe_2$@(1D)CNT exhibited the highest surface area, which is associated with the intrinsically high surface area of 1D CNT even before HEMM.

Microscopic morphologies of $MoSe_2$ and (2D)$MoSe_2$@(2D)Gr were further investigated by TEM (Fig. 5). The high-resolution image in Fig. 5a shows distinct lattice fringes of $MoSe_2$ where the interlayer spacings of 0.65 nm and 0.28 nm correspond to the (002) and (100) planes of $MoSe_2$, respectively. In the case of (2D)$MoSe_2$@(2D)Gr composite, the (002) plane of graphite is observed, in addition to several lattice planes of $MoSe_2$ (Fig. 5b). The number of $MoSe_2$ layers is estimated to be typically in the range of 15–20 layers in (2D)$MoSe_2$@(2D)Gr. Furthermore, the $MoSe_2$ domains are distributed well around the graphite matrices in the (2D)$MoSe_2$@(2D)Gr nanocomposite (see the boundary of $MoSe_2$ and graphite domains in Fig. 5b), which allows graphite to efficiently act as a buffer against the volume expansion of $MoSe_2$ during the electrochemical reaction. Additionally, EDS elemental mapping images reveal that distributions of the different atomic elements (Mo, Se, and C) overlap each another throughout the selected area in (2D)$MoSe_2$@(2D)Gr, indicating very good mixing of the two components and the homogenous distribution of $MoSe_2$ and graphite (Fig. 5c).

The lithiation/delithiation reactions of (2D)$MoSe_2$ and (2D)$MoSe_2$@(2D)Gr at the 1st, 2nd, and 3rd cycles were analyzed in the voltage range 0.01–3.00 V (vs. Li/Li^+) by CV (Fig. 6). The CV curves of $MoSe_2$ and (2D)$MoSe_2$@(2D)Gr are almost identical except for the relatively higher current observed for the (2D)$MoSe_2$@(2D)Gr composite. For both (2D)$MoSe_2$ and (2D)$MoSe_2$@(2D)Gr, the observed values for voltages at which the electrochemical reactions take place, are consistent with those in previously reported studies [17–19,21–23,35,36,42–46]. At the 1st cycle, three reduction peaks at 0.83 V, 0.3 V and 0.17 V are observed, which correspond to Li ion insertion into the interlayer spacing of $MoSe_2$ accompanied by a phase transition from 2H-$MoSe_2$ to 1 T-Li_xMoSe_2 at 0.83 V (Eq. (1)), the conversion to Mo and Li_2Se at 0.3 V, and Li ion insertion into the layered graphitic carbon at 0.17 V [28]. In addition, the solid electrolyte interface (SEI) layer is formed at 0.3 V and 0.17 V [44,47,48]. During the 2nd cycle, the peaks at 0.83 V, 0.3 V, and 0.17 V do not reappear, but new reduction peaks are seen at ~1.8 V and ~1.3 V, corresponding to the formation of Li_2Se from Se, and three oxidation peaks are observed at 0.2 V, 1.7 V, and 2.1 V. The peak at 0.2 V is related to the extraction of Li ions from the layered graphitic carbon [28], and the other two oxidation peaks at 1.7 V and 2.1 V correspond, respectively, to the oxidation of Mo to $MoSe_2$ [1,28]. The overall reaction occurring in the following cycles can be described as [36,49]:

$$MoSe_2 + 4Li^+ + 4e^- \leftrightarrow Mo + 2Li_2Se \quad (1)$$

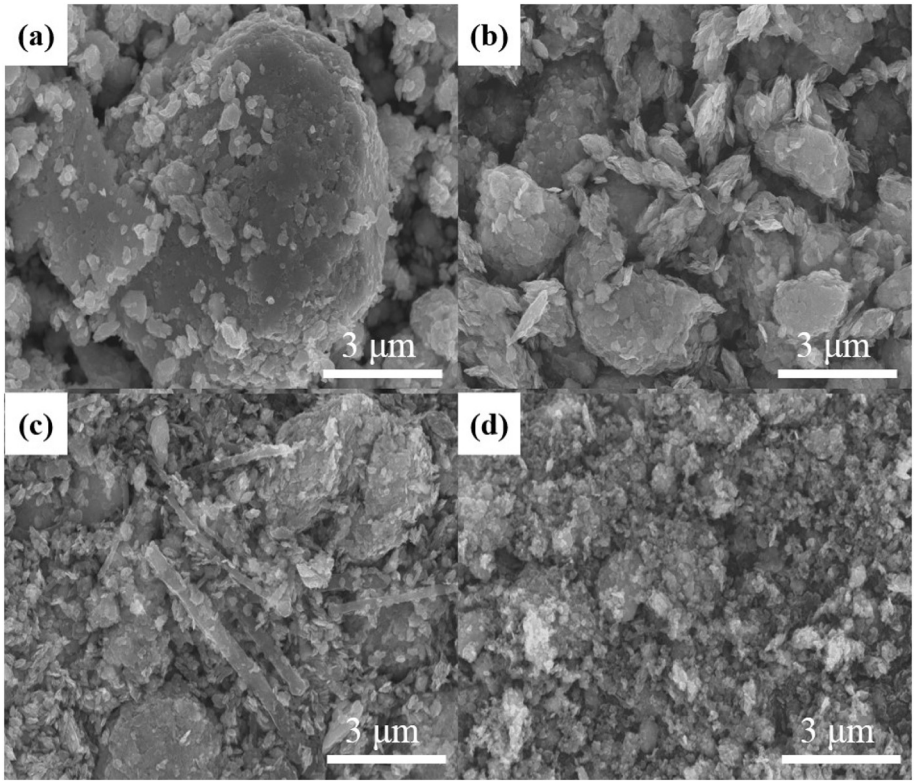

Fig. 3. SEM images of (a) (2D)$MoSe_2$, (b) (2D)$MoSe_2$@(2D)Gr, (c) (2D)$MoSe_2$@(0D)C, and (d) (2D)$MoSe_2$@(1D)CNT after HEMM.

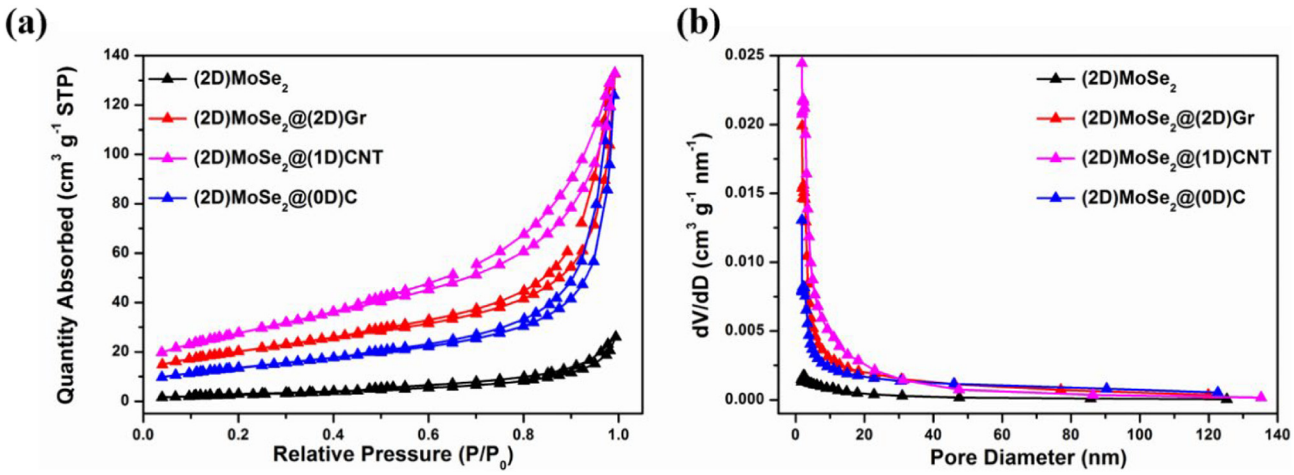

Fig. 4. N_2 adsorption-desorption isotherms of $MoSe_2$ and $MoSe_2$-carbon composites (a) surface area and (b) pore size distribution after HEMM.

Table 1
Surface area of (2D)$MoSe_2$, (2D)$MoSe_2$@(2D)Gr, (2D)$MoSe_2$@(1D)CNT, and (2D)$MoSe_2$@(0D)C before and after HEMM.

	BET surface area before HEMM ($m^2\,g^{-1}$)	BET surface area after HEMM ($m^2\,g^{-1}$)
(2D)$MoSe_2$	4.58	11.14
(2D)$MoSe_2$@(2D)Gr	3.43	70.68
(2D)$MoSe_2$@(1D)CNT		99.10
(2D)$MoSe_2$@(0D)C		48.34

Additionally, we analyzed the differential capacity plots (DCP) for the 1st, 2nd, 3rd, 30th and 50th cycles for both $MoSe_2$ and $MoSe_2$-carbon composites electrodes (Fig. S2). The peak positions observed in the DCP plots of both the electrodes are largely similar to those observed in the CV curves. Upon comparing the tendencies of the peaks for the different electrodes tested, a distinctly different behavior is observed for (2D)$MoSe_2$@(2D)Gr. For example, in contrast to other electrodes, the peak intensities gradually increase with the cycle number for the (2D)$MoSe_2$@(2D)Gr electrode, resulting in an increase in capacity with cycle number (Fig. S2b). This behavior can be attributed to i) the increased number of reactive sites on the $MoSe_2$ electrode to effectively bind to the electrolyte, owing to greater degree of activation in $MoSe_2$ and ii) the trapping of lithium ions at defect sites present in the $MoSe_2$ layer with the increase in cycle number [16,17,20,21,46–48].

With regard to the other electrodes, with an increase in the cycle number, the peak positions for the (2D)$MoSe_2$@(1D)CNT, (2D)$MoSe_2$@(0D)C, and (2D)$MoSe_2$ electrodes are either shifted to high (or low) voltages, or the electrodes become unstable and a total collapse is

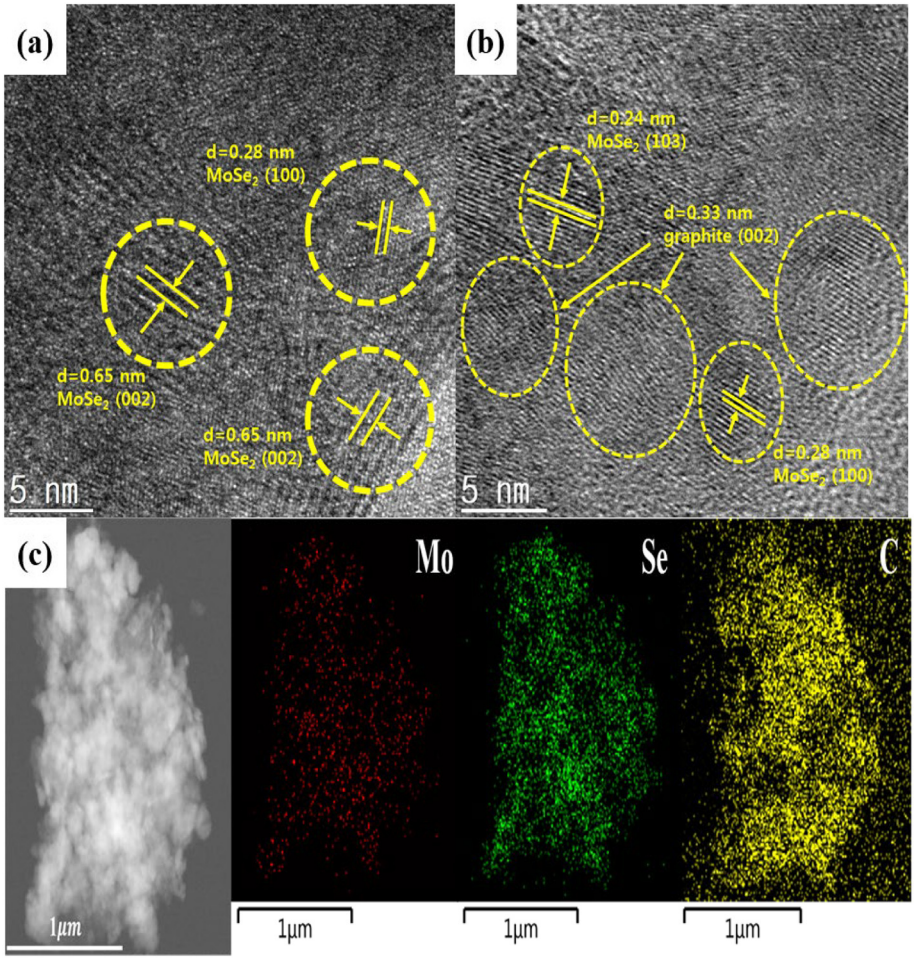

Fig. 5. TEM images of ball-milled (a) (2D)$MoSe_2$, (b) (2D)$MoSe_2$@(2D)Gr, and (c) EDS mapping images of (2D)$MoSe_2$@(2D)Gr.

observed. For example, the peaks for (2D)$MoSe_2$@(1D)CNT and (2D)$MoSe_2$@(0D)C electrodes show a shift from 2.1 V to 2.2 V, and for (2D)$MoSe_2$ electrode, the peak is shifted to 2.3 V at the 30th cycle in the charge sweep. At the 50th cycle, the peak of the (2D)$MoSe_2$@(0D)C electrode is shifted to 2.5 V, but that of the (2D)$MoSe_2$ electrode shows a collapse. However, the initial discharge peaks observed at 1.8 V for (2D)$MoSe_2$@(1D)CNT and (2D)$MoSe_2$@(0D)C electrodes are reduced to 1.75 V and 1.65 V, respectively. Furthermore, at the 50th cycle, all the discharge peaks of (2D)$MoSe_2$ show near-total collapse. These results indicate that the (2D)$MoSe_2$@(1D)CNT, (2D)$MoSe_2$@(0D)C, and (2D)$MoSe_2$ electrodes become unstable and cease to be functional during long-term operation.

Fig. 7 displays the charge/discharge voltage profiles of (2D)$MoSe_2$, (2D)$MoSe_2$@(2D)Gr, (2D)$MoSe_2$@1D CNT, and (2D)$MoSe_2$@(0D)C in the 1st, 2nd, 3rd, 30th, and 50th cycles at a current density of 100 mA g^{-1}. The plateaus of the voltage profile, in general, are in good agreement with the distinct peaks observed in the corresponding CV curves (Fig. 6). For all the electrodes, distinct voltage plateaus at 1.7 V and 2.1 V are observed during the initial charge sweep. The irreversible capacity loss after the 1st cycle is related to the formation of the SEI layers. As shown in Fig. 7a, the bare $MoSe_2$ electrode delivers initial discharge/charge capacities of 544 mAh g^{-1} and 455 mAh g^{-1},

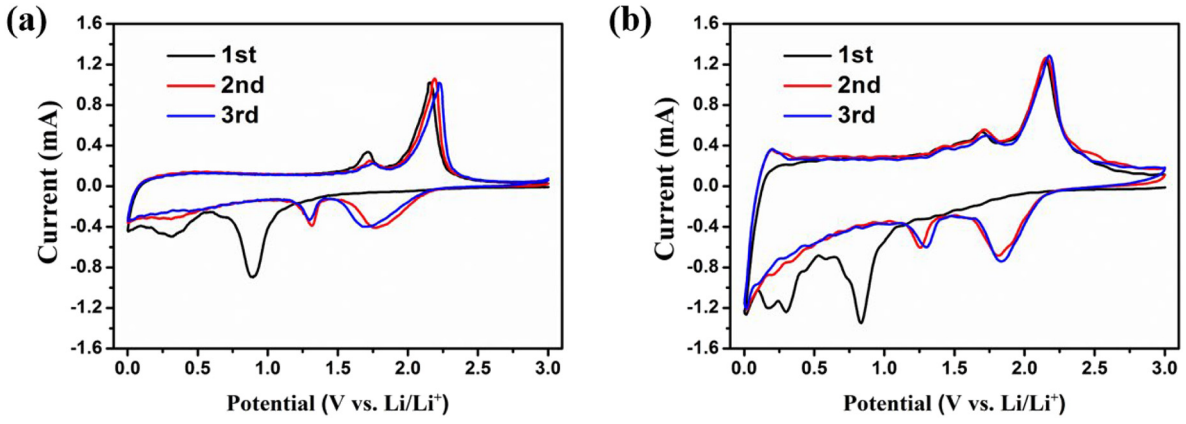

Fig. 6. Cyclic voltammograms of (a) (2D)$MoSe_2$ and (b) (2D)$MoSe_2$@(2D)Gr.

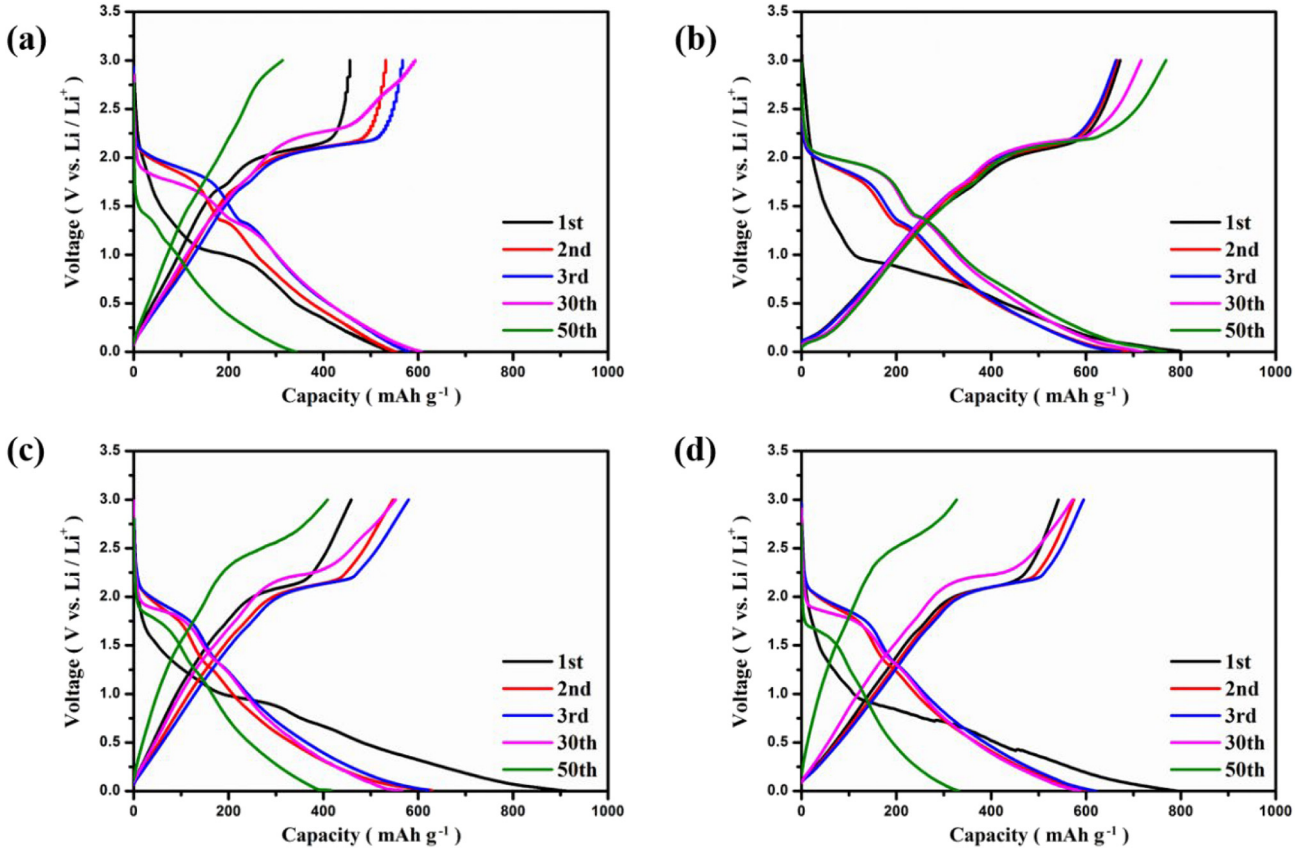

Fig. 7. Voltage profiles of (a) (2D)$MoSe_2$, (b) (2D)$MoSe_2$@(2D)Gr, (c) (2D)$MoSe_2$@(1D)CNT, and (d) (2D)$MoSe_2$@(0D)C at a current density of 100 mAh g^{-1} in the voltage range 0.01–3.0 V.

respectively. During cycling, the discharge/charge capacities of the $MoSe_2$ electrode increase until the 30th cycle, but decrease significantly at the 50th cycle. In contrast, the (2D)$MoSe_2$@(2D)Gr electrode delivers higher discharge/charge capacities of 799 and 671 mAh g^{-1} (Fig. 7b) and also shows a steady increase in capacity with increasing cycle number even until the 50th cycle. The discharge/charge capacities delivered by (2D)$MoSe_2$@1D CNT and (2D)$MoSe_2$@(0D)C at the 1st cycle are 910 and 458 mAh g^{-1} and 794 and 541 mAh g^{-1}, respectively (Fig. 7c and d). Both the electrodes deliver high initial discharge capacities but show poor coulombic efficiency (50% for 2D $MoSe_2$@1D CNT and 68% for 2D $MoSe_2$@0D C) at the 1st cycle; moreover, their capacities are severely diminished at the 50th cycle (Fig. 7c and d).

Fig. 8 presents the long-term cyclic performances and coulombic efficiencies for electrodes with different carbonaceous matrices and with different milling times when cycled in the voltage range 0.01–3.00 V at a current density of 100 mAh g^{-1}. The (2D)$MoSe_2$, (2D) MoSe2@(2D)Gr, (2D)$MoSe_2$@(1D)CNT, and (2D)$MoSe_2$@(0D)C electrodes exhibit initial discharge capacities of 545, 799, 794, and 910 mAh g^{-1} with coulombic efficiencies of 84, 84, 68, and 50%, respectively, (Fig. 8a). Notably, in the 2nd, 30th and the 200th cycles, the corresponding discharge capacities of the (2D)$MoSe_2$@(2D)Gr electrode are 687, 719, and 909 mAh g^{-1} (thereby showing a retention of 132%). In contrast, (2D)$MoSe_2$, (2D)$MoSe_2$@(1D)CNT, and (2D)$MoSe_2$@(0D)C electrodes exhibit a significant decrease in discharge capacities, especially after the 30th cycle (See Table 2 for the detailed specific capacity and capacity retention at different cycle numbers for (2D)$MoSe_2$, (2D)$MoSe_2$@(1D)CNT, and (2D)$MoSe_2$@(0D)C electrodes). This result demonstrates that the (2D)$MoSe_2$@(2D)Gr electrode exhibits the best cyclic performance during long-term operation, among all the $MoSe_2$-based electrodes tested in this study.

Additionally, the cyclic performance of (2D)$MoSe_2$@(2D)Gr (the best sample) was tested as a function of milling time (Fig. 8b). It should be noted that if the milling time is too short, the mixing between $MoSe_2$ and graphite will not be effective; however, under excessively long milling times, the electrode material can be damaged due to the application of high amounts of mechanical energy on $MoSe_2$ and graphite. Indeed, as shown in Fig. 8b, for milling times < 48 h (1, 12, 24, 36 h) the electrode shows a dramatic capacity loss in the earlier stages of cycling. However, as expected, unreasonably long milling times (60 h) similarly reduced the cyclic performance of the electrode. Thus, the sample milled for 48 h shows a steadily increasing capacity up to ~140 cycles, after which it has a stable performance. The increased capacity can be attributed to the increased contact area of the electrode with the electrolyte, which in turn is associated with the partial structural decomposition of the $MoSe_2$ electrode and the activation of $MoSe_2$ resulting from the reversible formation of a polymeric gel-like film [19,46,50]. We hypothesize the effect of milling time on the morphology and physical properties of (2D)$MoSe_2$@(2D)Gr as follows: (i) when longer milling time is applied, higher energy is generated which leads to the size reduction for the particles (i.e., increase in surface area that can be measured by BET), (ii) more exfoliation of 2D materials can occur due to the solid lubrication when increasing the milling time, (iii) the structure of materials can be damaged to form amorphous structure if too much energy is applied. These behaviors can significantly impact on the electrochemical performances of (2D)$MoSe_2$@(2D)Gr by the different milling time (1, 12, 24, 36, 48, and 60 h). In order to understand why the samples milled for 48 h showed the distinctively better performances compared with other cases (1, 12, 24, 36, and 60 h of milling conditions), we performed additional characterizations such as Raman, HRTEM, BET, and XRD. According to the Raman spectroscopy results for 1, 36, 48, and 60 h-milled (2D)$MoSe_2$@(2D)Gr (Fig. S3a), the values of Δ (Δ = difference in Raman shift between A_{1g} and E_{2g})

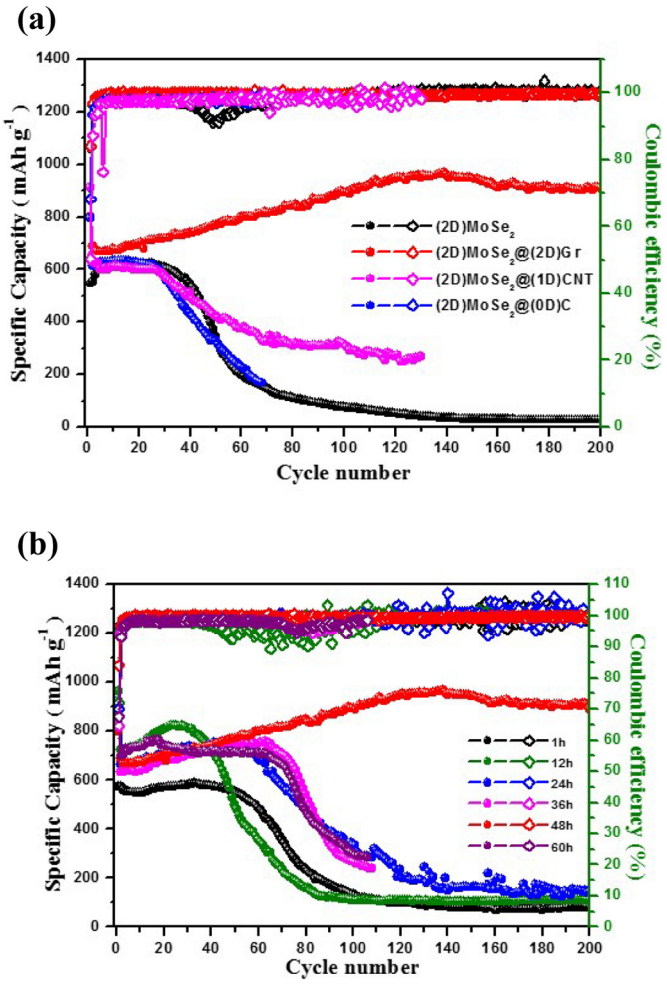

Fig. 8. Cyclic performance and coulombic efficiency of (a) ball-milled $MoSe_2$ and $MoSe_2$-carbon composites and (b) (2D)$MoSe_2$@(2D)Gr for different milling times (1, 12, 24, 36, 48, and 60 h) in the voltage range of 0.01–3.0 V at a current density of 100 mAh g^{-1}.

Table 2
Comparison of the specific capacity (2nd, 30th, and 200th) and the percentage capacity retention (2nd cycle/200th cycle).

Electrodes	Specific capacity (mAh g^{-1})			
	2nd	30th	200th	Capacity retention (2nd/200th) (%)
(2D)$MoSe_2$	552	607	28	5
(2D)$MoSe_2$@(2D)Gr	687	719	909	132
(2D)$MoSe_2$@(1D)CNT	613	578		N/A
(2D)$MoSe_2$@(0D)C	628	575		N/A

remained unchanged (Δ = 54) when milling time increased from 1 h to 36 h, indicating that the exfoliation of $MoSe_2$ is in the similar level (It has been known that Δ is proportional to the number of layers in $MoSe_2$). However, the samples under longer milling time (48 h and 60 h milling) showed significantly decreased Δ value (Δ = 37), indicating the strong exfoliation by the solid lubrication happened after the milling time of 48 h. The significant exfoliation of $MoSe_2$ after the milling time of 48 h is further confirmed by both HRTEM and BET results. As shown in Fig. S4, the number of $MoSe_2$ (002) layers are measured to be 45–50 layers for 36 h-milling sample and 15–20 layers for both 48 h- and 60 h-milling samples, respectively. Moreover, the BET analyses revealed the surface area of 45.4, 70.7 and 73.9 $m^2 g^{-1}$ for the milling time of 36 h, 48 h, and 60 h, respectively (Fig. S5), which gives the evidences of drastic increase in surface area from 36 h to 48 h milling time due to the significant decrease in the number of layers in $MoSe_2$. The results from Raman, HRTEM, and BET all consistently support the pronounced enhancement of electrochemical performances from 36 h to 48 h milling time for (2D)$MoSe_2$@(2D)Gr electrode. On the other hand, the deterioration of performances of (2D)$MoSe_2$@(2D)Gr from 48 h to 60 h milling can be explained by Raman and XRD results (Fig. S3). While I_D/I_G value increased from < 0.1 to ~0.44 when milling time increased from 1 h to 36 h, I_D/I_G value remained almost the same between 36 h (~0.44) and 48 h (~0.46) of milling, indicating there is no significant increase in defect densities from 36 h to 48 h of milling. However, at 60 h of milling, I_D/I_G value radically increased to 0.95 (almost 2-fold increase compared with 48 h case), meaning that the graphite is severely damaged. Furthermore, this phenomenon is consistently confirmed by XRD results (Fig. S3b) where the intensities of main peaks at 31.4° (002), 37.8° (100), 47.4° (103), 55.9° (105) for $MoSe_2$ are all significantly reduced, indicating the significant damage in $MoSe_2$ structure. Consequently, these Raman and XRD results explain why the electrochemical performance of (2D)$MoSe_2$@(2D)Gr at 60 h-milling is tremendously deteriorated.

Moreover, the (2D)$MoSe_2$@(2D)Gr electrode displays an excellent rate performance. Fig. 9a presents the rate capabilities of the $MoSe_2$ and $MoSe_2$-carbon composite electrodes at different current densities of 100, 500, 1000, and 3000 mA g^{-1}. At all current densities, (2D)$MoSe_2$@(2D)Gr shows a superior rate capability as compared with other electrodes. At 100 mA g^{-1}, in the first 5 cycles, (2D)$MoSe_2$, (2D)$MoSe_2$@(2D)Gr, (2D)$MoSe_2$@(1D)CNT, and (2D)$MoSe_2$@(0D)C deliver average discharge capacities of 572, 616, 634, and 571 mAh g^{-1}, respectively. Even though (2D)$MoSe_2$@(1D)CNT delivers a higher discharge capacity (associated with the very high surface area of (2D)$MoSe_2$@(1D)CNT after HEMM, as revealed by BET analysis) than (2D)$MoSe_2$@(2D)Gr, it shows a greater decrease in capacity at the current density of 500 mA g^{-1}. At current densities > 500 mA g^{-1}, the (2D)$MoSe_2$@(2D)Gr electrode consistently shows a superior rate capability as compared to all other electrodes. Even at the highest current density (3000 mA g^{-1}), the (2D)$MoSe_2$@(2D)Gr electrode delivers a capacity of 611 mAh g^{-1} (in comparison, the (2D)$MoSe_2$, (2D)$MoSe_2$@(1D)CNT, and (2D)$MoSe_2$@(0D)C electrodes delivered discharge capacities of, 353, 544, and 381 mAh g^{-1}, respectively). Thus, the capacity retention at 3000 mA g^{-1} is 5, 99, 67, and 86% for (2D)$MoSe_2$, (2D)$MoSe_2$@(2D)Gr, (2D)$MoSe_2$@(1D)CNT, and (2D)$MoSe_2$@(0D)C (Fig. S6), respectively. Remarkably, when the current density is reduced back to 1000 mA g^{-1}, the (2D)$MoSe_2$@(2D)Gr electrode still delivers a stable discharge capacity of 711 mAh g^{-1} until 50 cycles. This result demonstrates the sustainable and superior specific capacity of the (2D)$MoSe_2$@(2D)Gr electrode even at high current densities. However, a certain amount of reduction in capacity could not be clearly observed with an increase in current density for (2D)$MoSe_2$@(2D)Gr electrode due to the increased capacities in initial stage as shown and discussed in Fig. 8. Therefore, the rate capability of that electrode should be tested when the cyclic performance becomes stable to see more clear behavior of rate capability. Fig. 9(b) presents the rate capability of (2D)$MoSe_2$@(2D)Gr electrode after 140 cycles of pre-cycling at 100 mA g^{-1} along with the rate capability without pre-cycling. The rate capability after pre-cycling showed the common reduction in capacity when current density increased, which were measured to be 900, 763, 650, and 472 mAh g^{-1} at the current densities of 100, 500, 1000, and 3000 mA g^{-1}, respectively. These capacities are still higher than those of other samples ((2D)$MoSe_2$@(1D)CNT, (2D)$MoSe_2$@(0D)C, and (2D)$MoSe_2$).

Furthermore, the long-term cycling performances of (2D)$MoSe_2$@(2D)Gr electrode at high current density of 1000 mA g^{-1} were measured to demonstrate the superior cyclic stability of our optimized electrode. As shown in Fig. 9(c), the stable cyclic performance throughout 200 cycles was confirmed even at this high current density

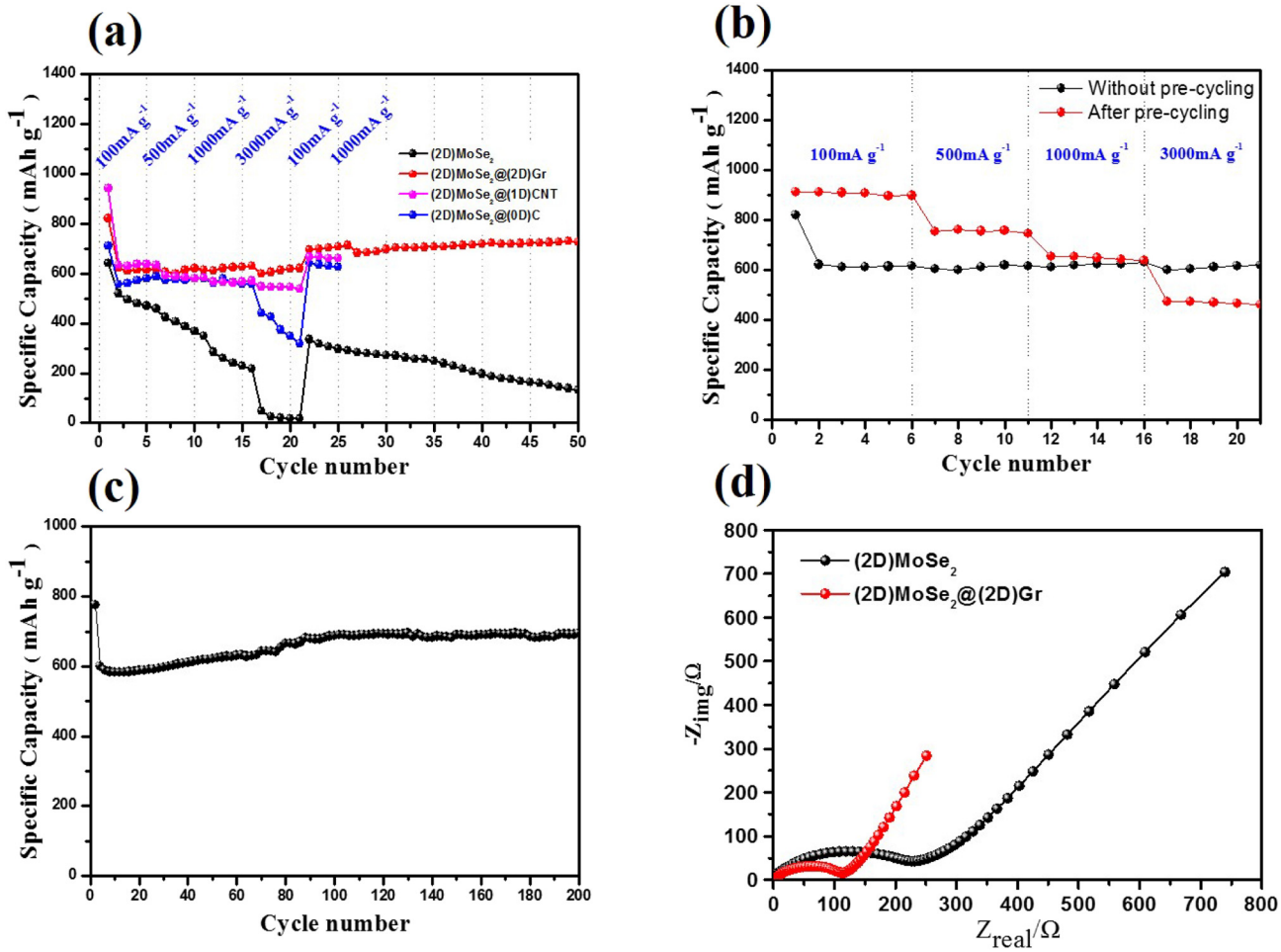

Fig. 9. (a) Discharge capacity of $MoSe_2$ and $MoSe_2$-carbon composites under different current densities in the range 100–3000 mA g^{-1}, (b) discharge capacity of (2D)$MoSe_2$@(2D)Gr under different current densities of 100–3000 mA g^{-1} with and without pre-cycling (140 cycles), (c) long-term cyclic performances of (2D)$MoSe_2$@(2D)Gr measured at 1000 mA g^{-1}, (d) Nyquist plots of (2D)$MoSe_2$ and (2D)$MoSe_2$@(2D)Gr after the 10th cycle.

(1000 mA g^{-1}) although there was a certain level of capacity reduction as compared to obtained capacities at 100 mA g^{-1}.

EIS were measured to further investigate the origin of the superior electrochemical performance of (2D)$MoSe_2$@(2D)Gr (Fig. 9b). In general, the curve obtained from EIS measurement is divided into three major regions, namely, the high-frequency, medium-frequency, and low-frequency regions, which correspond to the SEI layer resistance R_f at high frequency, charge transfer resistance of the electrode-electrolyte interface R_{ct} at medium frequency, and Warburg impedance Z_w related to the diffusivity of the lithium ion during cycling at low frequency [3,24,46,51]. Clearly, at high to medium frequencies, (2D)$MoSe_2$@(2D)Gr exhibits a smaller semicircle than (2D)$MoSe_2$, which implies that the addition of graphite significantly reduces the charge transfer resistance (R_{ct}). Moreover, in the low-frequency region, the vertical slope for (2D)$MoSe_2$@(2D)Gr is steeper than that for (2D)$MoSe_2$, indicating an enhanced lithium ion diffusion path [39] As a result of these two effects, the electrochemical performance of the (2D)$MoSe_2$@(2D)Gr electrode is enhanced.

To investigate the morphological change of the electrode surface during long-term operation, we disassembled the cells after 200 cycles in an Ar-filled glove box and inspected the surfaces of (2D)$MoSe_2$ and (2D)$MoSe_2$@(2D)Gr by SEM. As shown in Fig. 10a, the (2D)$MoSe_2$ electrode shows severe aggregation along with cracks due to its failure to withstand large volume changes during repeated charging and discharging. In contrast, the (2D)$MoSe_2$@(2D)Gr electrode largely retains its initial structure without any evidence of aggregations, cracks, or pulverization after 200 cycles, indicating a better cycle stability than the (2D)$MoSe_2$ electrode (Fig. 10b). This ex-situ SEM image provides further visual proof of the superiority of the novel (2D)$MoSe_2$@(2D)Gr electrode developed in this work.

4. Conclusions

In summary, we studied various $MoSe_2$-based electrodes prepared using a scalable HEMM method for use as anodes in LIBs. Among the different $MoSe_2$-carbon nanocomposites, ((2D)$MoSe_2$@(2D)Gr, (2D)$MoSe_2$@(1D)CNT, and (2D)$MoSe_2$@(0D)C), the best electrochemical performance was exhibited by (2D)$MoSe_2$@(2D)Gr. The superiority of (2D)$MoSe_2$@(2D)Gr results from the homogeneous distribution of 2D $MoSe_2$ in the 2D graphite matrix, which in turn is facilitated by the lubrication effect of graphite during HEMM; this effect is confirmed from the results of XRD, Raman, BET, SEM, and TEM analyses. Thus, graphite effectively mitigated the effect of volume change of $MoSe_2$ during the lithiation/delithiation process by maintaining its crystal structure. As a result, (2D)$MoSe_2$@(2D)Gr delivered discharge and charge capacities of 799 and 671 mAh g^{-1} with a coulombic efficiency of 84.0%; this performance is by far better than that observed for other types of $MoSe_2$-carbon nanocomposites as well as bare $MoSe_2$. The stable cycle performance was further confirmed from EIS and ex-situ SEM. In conclusion, our new electrode (prepared from (2D)$MoSe_2$@(2D)Gr) developed by a scalable HEMM process is expected to be a promising anode material for LIBs in the future.

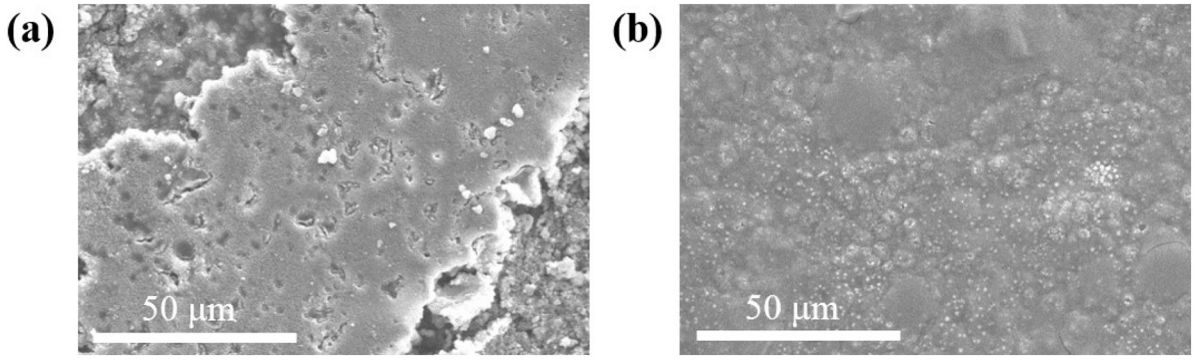

Fig. 10. Ex-situ SEM images of (a) (2D)$MoSe_2$ and (b) (2D)$MoSe_2$@(2D)Gr after 200 cycles.

Acknowledgments

This research was supported by the Basic Science Research Program through the National Research Foundation of Korea (NRF) funded by the Ministry of Education (NRF-2016R1D1A1B03931903). This research was supported by Nano·Material Technology Development Program through the National Research Foundation of Korea (NRF) funded by the Ministry of Science, ICT and Future Planning (2009-0082580).

Appendix A. Supplementary data

Supplementary data to this article can be found online at https://doi.org/10.1016/j.apsusc.2019.03.165.

References

[1] X. Yang, Z. Zhang, Y. Fu, Q. Li, Porous hollow carbon spheres decorated with molybdenum diselenide nanosheets as anodes for highly reversible lithium and sodium storage, Nanoscale 7 (2015) 10198–10203.
[2] D.J. Sathe, P.A. Chate, Hexagonal nanosized molybdenum diselenide thin film deposited at 333 K by chemical method, Solid State Sci. 48 (2015) 19–22.
[3] Y. Yan, B. Sun, D. Ma, Resistive switching memory characteristics of single $MoSe_2$ nanorods, Chem. Phys. Lett. 638 (2015) 103–107.
[4] C. Tsai, K. Chan, F. Abild-Pedersen, J.K. Norskov, Active edge sites in $MoSe_2$ and WSe_2 catalysts for the hydrogen evolution reaction: a density functional study, Phys. Chem. Chem. Phys. 16 (2014) 13156–13164.
[5] Y. Huang, H. Lu, H. Gu, J. Fu, S. Mo, C. Wei, Y.-E. Miao, T. Liu, A CNT@$MoSe_2$ hybrid catalyst for efficient and stable hydrogen evolution, Nanoscale 7 (2015) 18595–18602.
[6] W. Yang, L. Gan, H. Li, T. Zhai, Two-dimensional layered nanomaterials for gas-sensing applications, Inorg. Chem. Front. 3 (2016) 433–451.
[7] D.J. Late, T. Doneux, M. Bougouma, Single-layer $MoSe_2$ based NH_3 gas sensor, Appl. Phys. Lett. 105 (2014) 233103.
[8] S. Hong, S.M. Kim, W.G. Song, Y. Hong, S. Kim, High-mobility 2D layered semiconducting transistors based on large-area and highly crystalline CVD-grown $MoSe_2$ for flexible electronics, in: 2016 IEEE Silicon Nanoelectronics Workshop (SNW), 2016, pp. 56–57.
[9] H.-J. Chuang, B. Chamlagain, M. Koehler, M.M. Perera, J. Yan, D. Mandrus, D. Tománek, Z. Zhou, Low-resistance 2D/2D Ohmic contacts: a universal approach to high-performance WSe_2, MoS_2, and $MoSe_2$ transistors, Nano Lett. 16 (2016) 1896–1902.
[10] J.-S. Rhyee, J. Kwon, P. Dak, J.H. Kim, S.M. Kim, J. Park, Y.K. Hong, W.G. Song, I. Omkaram, M.A. Alam, S. Kim, High-mobility transistors based on large-area and highly crystalline CVD-grown $MoSe_2$ films on insulating substrates, Adv. Mater. 28 (2016) 2316–2321.
[11] K. Furlan, D. Consoni, B. Leite, M. V G Dias, A. Klein, Microstructural characterization of solid state reaction phase formed during sintering of hexagonal boron nitride with iron, Microsc. Microanal., 23 (2017) 1061–1066.
[12] C. Fan, Z. Wei, S. Yang, J. Li, Synthesis of $MoSe_2$ flower-like nanostructures and their photo-responsive properties, RSC Adv. 4 (2014) 775–778.
[13] W. Zhang, Y. Cao, P. Tian, F. Guo, Y. Tian, W. Zheng, X. Ji, J. Liu, Soluble, exfoliated two-dimensional nanosheets as excellent aqueous lubricants, ACS Appl. Mater. Interfaces 8 (2016) 32440–32449.
[14] Y. Zhang, Z. Liu, H. Zhao, Y. Du, $MoSe_2$ nanosheets grown on carbon cloth with superior electrochemical performance as flexible electrode for sodium ion batteries, RSC Adv. 6 (2016) 1440–1444.
[15] A. Eftekhari, Molybdenum diselenide ($MoSe_2$) for energy storage, catalysis, and optoelectronics, Appl. Mater. Today 8 (2017) 1–17.
[16] Y. Zhang, A. Pan, L. Ding, Z. Zhou, Y. Wang, S. Niu, S. Liang, G. Cao, Nitrogen-doped yolk–shell-structured CoSe/C dodecahedra for high-performance sodium ion batteries, ACS Appl. Mater. Interfaces 9 (2017) 3624–3633.
[17] Z. Zhang, Y. Fu, X. Yang, Y. Qu, Z. Zhang, Hierarchical $MoSe_2$ nanosheets/reduced graphene oxide composites as anodes for lithium-ion and sodium-ion batteries with enhanced electrochemical performance, ChemNanoMat 1 (2015) 409–414.
[18] L. Ma, X. Zhou, L. Xu, X. Xu, L. Zhang, W. Chen, Ultrathin few-layered molybdenum selenide/graphene hybrid with superior electrochemical Li-storage performance, J. Power Sources 285 (2015) 274–280.
[19] Z. Luo, J. Zhou, L. Wang, G. Fang, A. Pan, S. Liang, Two-dimensional hybrid nanosheets of few layered $MoSe_2$ on reduced graphene oxide as anodes for long-cycle-life lithium-ion batteries, J. Mater. Chem. A 4 (2016) 15302–15308.
[20] D. Xie, W. Tang, Y. Wang, X. Xia, Y. Zhong, D. Zhou, D. Wang, X. Wang, J. Tu, Facile fabrication of integrated three-dimensional C-$MoSe_2$/reduced graphene oxide composite with enhanced performance for sodium storage, Nano Res. 9 (2016) 1618–1629.
[21] Y. Liu, M. Zhu, D. Chen, Sheet-like $MoSe_2$/C composites with enhanced Li-ion storage properties, J. Mater. Chem. A 3 (2015) 11857–11862.
[22] Y. Shi, C. Hua, B. Li, X. Fang, C. Yao, Y. Zhang, Y.-S. Hu, Z. Wang, L. Chen, D. Zhao, G.D. Stucky, Highly ordered mesoporous crystalline $MoSe_2$ material with efficient visible-light-driven photocatalytic activity and enhanced lithium storage performance, Adv. Funct. Mater. 23 (2013) 1832–1838.
[23] L. Wu, P. Tan, Y. Liu, Y. Shang, W. Liu, X. Xiong, J. Pan, In situ formation of carbon encapsulated nanosheet-assembled $MoSe_2$ hollow nanospheres with boosting lithium storage, J. Colloid Interface Sci. 491 (2017) 279–285.
[24] Y.N. Ko, S.H. Choi, S.B. Park, Y.C. Kang, Hierarchical $MoSe_2$ yolk-shell microspheres with superior Na-ion storage properties, Nanoscale 6 (2014) 10511–10515.
[25] S.H. Choi, Y.C. Kang, Fullerene-like $MoSe_2$ nanoparticles-embedded CNT balls with excellent structural stability for highly reversible sodium-ion storage, Nanoscale 8 (2016) 4209–4216.
[26] Q. Su, X. Cao, X. Kong, Y. Wang, C. Peng, J. Chen, B. Yin, J. Shi, S. Liang, A. Pan, Carbon-encapsulated $MoSe_2$/C nanorods derived from organic-inorganic hybrid enabling superior lithium/sodium storage performances, Electrochim. Acta 292 (2018) 339–346.
[27] M. Zhu, Z. Luo, A. Pan, H. Yang, T. Zhu, S. Liang, G. Cao, N-doped one-dimensional carbonaceous backbones supported MoSe 2 nanosheets as superior electrodes for energy storage and conversion, Chem. Eng. J. 334 (2018) 2190–2200.
[28] H. Zhao, H. Zeng, Y. Wu, S. Zhang, B. Li, Y. Huang, Facile scalable synthesis and superior lithium storage performance of ball-milled MoS_2-graphite nanocomposites, J. Mater. Chem. A 3 (2015) 10466–10470.
[29] D. Berman, A. Erdemir, A.V. Sumant, Graphene: a new emerging lubricant, Mater. Today 17 (2014) 31–42.
[30] K.P. Furlan, D.R. Consoni, B. Leite, M.V.G. Dias, A.N. Klein, Microstructural characterization of solid state reaction phase formed during sintering of hexagonal boron nitride with Iron, Microsc. Microanal. 23 (2017) 1061–1066.
[31] J.C. Spear, B.W. Ewers, J.D. Batteas, 2D-nanomaterials for controlling friction and wear at interfaces, Nano Today 10 (2015) 301–314.
[32] J. Guichong, W. Huanwen, C. Dongliang, H. Haiyong, T. Nguyen Huy, Z. Yongqi, Z. Zheng, F. Hong Jin, Ultrathin $MoSe_2$ @N-doped carbon composite nanospheres for stable Na-ion storage, Nanotechnology, 28 (2017) 42LT01.
[33] J. Zhang, W. Kang, M. Jiang, Y. You, Y. Cao, T.-W. Ng, D.Y.W. Yu, C.-S. Lee, J. Xu, Conversion of 1T-MoS_2 to 2H-$MoS_{2x}Se_{2-2x}$ mesoporous nanospheres for superior sodium storage performance, Nanoscale 9 (2017) 1484–1490.
[34] Z. Liu, Y. Zhang, H. Zhao, N. Li, Y. Du, Constructing monodispersed $MoSe_2$ anchored on graphene: a superior nanomaterial for sodium storage, Sci. China Mater. 60 (2017) 167–177.
[35] W. Tang, D. Xie, T. Shen, X. Wang, D. Wang, X. Zhang, X. Xia, J. Wu, J. Tu, Construction of nitrogen-doped carbon-coated $MoSe_2$ microspheres with enhanced performance for lithium storage, Chem. Eur. J. 23 (2017) 12924–12929.
[36] C. Zheng, C. Chen, L. Chen, M. Wei, A CMK-5-encapsulated $MoSe_2$ composite for rechargeable lithium-ion batteries with improved electrochemical performance, J. Mater. Chem. A 5 (2017) 19632–19638.
[37] Y. Tang, Z. Zhao, Y. Wang, Y. Dong, Y. Liu, X. Wang, J. Qiu, Carbon-stabilized interlayer-expanded few-layer MoSe2 nanosheets for sodium ion batteries with enhanced rate capability and cycling performance, ACS Appl. Mater. Interfaces 8 (2016) 32324–32332.

[38] J. Li, Y. Hou, X. Gao, D. Guan, Y. Xie, J. Chen, C. Yuan, A three-dimensionally interconnected carbon nanotube/layered MoS2 nanohybrid network for lithium ion battery anode with superior rate capacity and long-cycle-life, Nano Energy 16 (2015) 10–18.

[39] D. Xie, X. Xia, Y. Zhong, Y. Wang, D. Wang, X. Wang, J. Tu, Exploring Advanced sandwiched arrays by vertical graphene and N-Doped carbon for enhanced sodium storage, Adv. Energy Mater., 7 (2017) 1601804-n/a.

[40] C. Brolly, J. Parnell, S. Bowden, Raman spectroscopy: caution when interpreting organic carbon from oxidising environments, Planet. Space Sci. 121 (2016) 53–59.

[41] M. Saffaripour, L.-L. Tay, K.A. Thomson, G.J. Smallwood, B.T. Brem, L. Durdina, M. Johnson, Raman spectroscopy and TEM characterization of solid particulate matter emitted from soot generators and aircraft turbine engines, Aerosol Sci. Technol. 51 (2017) 518–531.

[42] B. Mendoza-Sánchez, J. Coelho, A. Pokle, V. Nicolosi, A study of the charge storage properties of a $MoSe_2$ nanoplatelets/SWCNTs electrode in a Li-ion based electrolyte, Electrochim. Acta 192 (2016) 1–7.

[43] Y. Yang, S. Wang, J. Zhang, H. Li, Z. Tang, X. Wang, Nanosheet-assembled $MoSe_2$ and S-doped $MoSe_{2-x}$ nanostructures for superior lithium storage properties and hydrogen evolution reactions, Inorg. Chem. Front. 2 (2015) 931–937.

[44] F.S. Pan, J.Q. Wang, Z.Z. Yang, L. Gu, Y. Yu, MoS_2-graphene nanosheet-CNT hybrids with excellent electrochemical performances for lithium-ion batteries, RSC Adv. 5 (2015) 77518–77526.

[45] X. Zhao, J. Sui, F. Li, H. Fang, H. Wang, J. Li, W. Cai, G. Cao, Lamellar $MoSe_2$ nanosheets embedded with MoO_2 nanoparticles: novel hybrid nanostructures promoted excellent performances for lithium ion batteries, Nanoscale 8 (2016) 17902–17910.

[46] H. Wu, Y. Wu, X. Chen, Y. Ma, M. Xu, W. Wei, J. Pan, X. Xiong, Rational design and preparation of few-layered $MoSe_2$ nanosheet@C/TiO_2 nanobelt heterostructures with superior lithium storage performance, RSC Adv. 6 (2016) 23161–23168.

[47] Y. Gong, S. Yang, L. Zhan, L. Ma, R. Vajtai, P.M. Ajayan, A bottom-up approach to build 3D architectures from nanosheets for superior lithium storage, Adv. Funct. Mater. 24 (2014) 125–130.

[48] Y. Gong, S. Yang, Z. Liu, L. Ma, R. Vajtai, P.M. Ajayan, Graphene-network-backboned architectures for high-performance lithium storage, Adv. Mater. 25 (2013) 3979–3984.

[49] X. Yang, Z. Zhang, X. Shi, Rational design of coaxial-cable $MoSe_2$/C: towards high performance electrode materials for lithium-ion and sodium-ion batteries, J. Alloys Compd. 686 (2016) 413–420.

[50] G.D. Park, J.H. Kim, S.-K. Park, Y.C. Kang, $MoSe_2$ embedded CNT-reduced graphene oxide composite microsphere with superior sodium ion storage and electrocatalytic hydrogen evolution performances, ACS Appl. Mater. Interfaces 9 (2017) 10673–10683.

[51] E. Allcorn, A. Manthiram, NiSb–Al_2O_3–C nanocomposite anodes with long cycle life for Li-ion batteries, J. Phys. Chem. C 118 (2014) 811–822.